Electrochemical Na Extraction/Insertion of Na 3 V 2 O 2x (PO 4) 2 F 3−2x

10 AUTHORS, INCLUDING:

Verónica Palomares
Universidad del País Vasco / Euskal Herriko U…
22 PUBLICATIONS   1,043 CITATIONS

SEE PROFILE

Javier Alonso Masa
University of South Florida
45 PUBLICATIONS   241 CITATIONS

SEE PROFILE

M. Luisa Fdez-Gubieda
Universidad del País Vasco / Euskal Herriko U…
116 PUBLICATIONS   727 CITATIONS

SEE PROFILE

Teofilo Rojo
Universidad del País Vasco / Euskal Herriko U…
554 PUBLICATIONS   9,337 CITATIONS

SEE PROFILE

Electrochemical Na Extraction/Insertion of Na$_3$V$_2$O$_{2x}$(PO$_4$)$_2$F$_{3-2x}$

Paula Serras,[†] Verónica Palomares,[†] Javier Alonso,[‡] Neeraj Sharma,[§] Juan Miguel López del Amo,[∇] Pierre Kubiak,[∇] María Luisa Fdez-Gubieda,[‡,⊥] and Teófilo Rojo*,[†,∇]

[†]Departamento de Química Inorgánica, Universidad del País Vasco UPV/EHU, Bilbao, Spain
[‡]BCMaterials, Edificio No. 500, Parque Tecnológico de Vizcaya, Derio, Spain
[§]School of Chemistry, The University of New South Wales, Sydney NSW 2052, Australia
[∇]CIC ENERGIGUNE, Parque Tecnológico de Álava, Albert Einstein 48, ED. CIC, 01510, Miñano, Spain
[⊥]Departamento de Electricidad y Electrónica, Universidad del País Vasco UPV/EHU, Bilbao, Spain

S *Supporting Information*

ABSTRACT: A mixed-valence V^{3+}/V^{4+} composite material belonging to the Na$_3$V$_2$O$_{2x}$(PO$_4$)-2F$_{3-2x}$/C family is synthesized and the electrochemical Na extraction/insertion mechanism is determined using a combination of high-resolution synchrotron X-ray diffraction (XRD) data, X-ray absorption spectroscopy (XAS), ^{23}Na and ^{19}F solid state nuclear magnetic resonance (NMR), double titration (for the elucidation of the vanadium oxidation state), and electrochemical measurements. The vanadium oxidation state is found to be +3.8 for the as-prepared sample. Detailed analysis of the cathode structural evolution illustrated that the V^{4+}/V^{5+} couple is active in this compound during electrochemical cycling between 2.8 V and 4.3 V. This study demonstrates how the sodium-ion extraction and insertion pathways in cathode materials can be followed (and verified) using several experimental techniques, especially when multiple potential oxidation states are present in the parent compound.

KEYWORDS: *sodium ion batteries, electrochemistry, mixed valence sodium vanadium fluorophosphate, X-ray diffraction and X-ray absorption near edge structure*
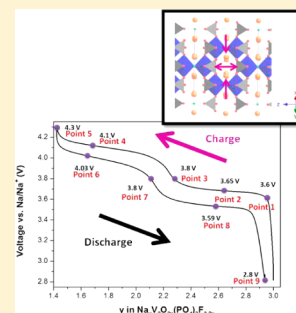
1. INTRODUCTION

There exists growing scientific and commercial interest in sodium-ion battery technology. Recent studies on applicable voltage ranges, electrode/electrolyte stability, and diffusion barriers of sodium-ion and lithium-ion battery materials indicate that sodium-ion systems can be competitive with lithium-ion systems.[1] This is mainly due to the natural abundance of sodium and its relatively lower price, compared to lithium.[2] The search for commercially viable sodium-ion batteries demands that new electrode materials and electrolytes be found and optimized, in order to obtain batteries that are more economic, safer, and have longer life.

Framework materials based on the phosphate polyanion have been identified as potential electroactive materials for sodium metal and sodium-ion battery applications, because of the strong inductive effect of the PO$_4^{3-}$ group. In particular, fluorophosphate materials possess even higher operating voltages, because the inductive effect of fluorine is added to the effect of phosphate.[3] The high operating voltages of fluorophosphate-based cathode materials provide a key advantage to solve the energy density challenges of sodium-based batteries.

In sodium–vanadium fluorophosphates, the existence of a mixed-valence family of compounds between Na$_3$V$_2$(PO$_4$)$_2$F$_3$ and Na$_3$(VO)$_2$(PO$_4$)$_2$F phases has been recently reported by our research group,[4] as well as by Park et al.[5] Thus, Na$_3$V$_2$(PO$_4$)$_2$F$_3$ and Na$_3$(VO)$_2$(PO$_4$)$_2$F represent extreme or

end-member compounds present in the +3 and +4 vanadium oxidation state, respectively, whereas intermediate compounds are V^{3+}/V^{4+} mixed-valence phases. In the general formula Na$_3$V$_2$O$_{2x}$(PO$_4$)$_2$F$_{3-2x}$ that we proposed ($x = 0$ for Na$_3$V$_2$(PO$_4$)$_2$F$_3$ and $x = 1$ for Na$_3$(VO)$_2$(PO$_4$)$_2$F), the vanadium oxidation state—and, therefore, the fluorine and oxygen content (x value)—varies according to the amount of remaining carbon in the material during synthesis.[4] Na$_3$(VO)$_2$(PO$_4$)$_2$F (V^{4+} phase) is obtained when there is no remaining carbon in the as-prepared sample. However, Na$_3$V$_2$(PO$_4$)$_2$F$_3$ (V^{3+} extreme) seems to be unstable, irrespective of the carbon proportions used. This fact can be attributed to the oxidizing atmosphere present in the vessel used in the hydrothermal method, where the carbon coating does not seem to be sufficient to stop the partial reduction of V^{3+}. A recent report concerning Na$_3$V$_2$(PO$_4$)$_2$F$_3$ (V^{3+} phase) using a different synthetic regime illustrated that the electrochemical activity was attributed to the V^{3+}/V^{4+} redox reaction,[6] but all mixed-valence compounds studied to date indicate that the electroactive redox couple corresponds to V^{4+}/V^{5+}.[4] In general, sodium−vanadium fluorophosphates (Na$_3$V$_2$O$_{2x}$(PO$_4$)$_2$F$_{3-2x}$) are good cathodic materials for sodium-ion batteries, because of their high reaction voltages (at 3.6 and 4.1 V vs. Na/Na$^+$) and their good specific capacity

values and cyclability in sodium half-cells. Current findings indicate that a moderate carbon percentage (∼6 wt %) and, hence, a V^{3+}/V^{4+} mixed valence in the as-prepared cathodes enhances electrochemical performance, because of the intrinsically better conductivity.[4] Therefore, the $Na_3V_2O_{2x}(PO_4)_2F_{3-2x}$ sample studied in this work is prepared by the hydrothermal method using a carbon-containing VPO_4 ceramic precursor resulting in 6.4 wt % carbon in the final product.[7] However, no detailed structural work has been undertaken to determine the sodium extraction/insertion mechanism of these materials, in light of their superior electrochemical performance. In addition, the ambiguity in the electroactive vanadium oxidation states must be resolved in order to design better compositions in this system. These aspects are addressed in this work, using information derived from several techniques, including high-resolution synchrotron X-ray diffraction (XRD), ^{23}Na and ^{19}F solid-state nuclear magnetic resonance (NMR), double titration for the determination of the vanadium oxidation state, ex situ XRD data of charged and discharged electrodes at selected voltages, X-ray absorption spectroscopy (XAS), and electrochemical measurements. These reveal the evolution of the vanadium oxidation state associated with the sodium-ion insertion/extraction and electrochemical properties in a sodium cell.

2. EXPERIMENTAL SECTION

$Na_3V_2O_{2x}(PO_4)_2F_{3-2x}$ was synthesized by the hydrothermal method from a ceramic precursor. The synthesis process took place in two steps. First, VPO_4/C composite was synthesized by the ceramic method. V_2O_5 (Sigma−Aldrich, 99.99% purity) and $NH_4H_2PO_4$ (Fluka, 99.5% purity) were mixed in an agate mortar in a stoichiometric ratio with a 25% molar excess of Kejten black. This mixture was annealed twice under nitrogen atmosphere at 300 and 850 °C. Second, a sodium fluorophosphate sample was prepared under mild hydrothermal conditions at 170 °C and autogenous pressure by reacting NaF (Sigma−Aldrich, 99% purity) and the VPO_4/C composite in a 3.3/1 molar proportion. The reaction mixture was sealed in a polytetrafluoroethylene (PTFE)-lined steel pressure vessel, which was maintained at 170 °C for 65 h.

Elemental analysis was performed using an Eurovector 3000 system. Powder X-ray diffraction (XRD) patterns were collected in a Bruker D8 Avance Vårio diffractometer working with Cu Kα radiation at room temperature. High-resolution synchrotron XRD data were collected on the powder diffraction beamline (10-BM-1)[8] at the Australian Synchrotron, using a wavelength of λ = 0.83696(2) Å, determined using the NIST SRM660a LaB_6 standard reference material. Powder samples were packed and sealed in 0.5 mm glass capillaries and data were collected for 6 min at ambient temperature, using Debye−Scherrer geometry. Rietveld refinements were carried out using the GSAS[9] software suite with the EXPGUI[10] software interface.

The ^{23}Na solid-state nuclear magnetic resonance (ssNMR) spectrum was recorded in a Bruker Avance III 500 spectrometer (11.7 T magnet), using the standard 1.3 mm Bruker MAS probe. The spinning speed was set to 50 kHz at room temperature. A single-pulse sequence was used, with 90° pulse duration of 1.3 μs and a recycle delay of 2 s. The ^{23}Na shift was referenced to 0.1 M NaCl (0 ppm). The ^{19}F spectra were recorded in a Bruker Avance III 200 MHz spectrometer (4.68 T) with 50 kHz MAS frequency in order to avoid interference with the rotational sidebands. A single pulse sequence was used, with a 90° pulse duration of 2 μs and a recycle delay of 5 s. The ^{19}F shift was referenced to solid LiF (−204 ppm). The recycle delay in this case was set to 3 s.

The quantification of the average oxidation state of vanadium (AV) was determined using a double titration method.[5] Vanadium-containing compounds were completely dissolved in a 2 M H_2SO_4 solution at 80 °C. The first titration with a 0.1 N $KMnO_4$ solution was

stopped when the overall color of the solution abruptly changed to red (corresponding to the complete oxidation of the unknown initial oxidation state $V^{?+}$ to V^{5+}) and the total volume of the $KMnO_4$ solution consumed during the first titration (V1) was measured. An excess amount of $FeSO_4(NH_4)_2(SO_4)\cdot6H_2O$ was added to the solution to reduce all V^{5+} ions to V^{4+} ions by the Fe^{2+}/Fe^{3+} redox couple. Then, an excess amount of $(NH_4)_2S_2O_8$ was added to fully oxidize residual Fe^{2+} to Fe^{3+} to ensure the accuracy of the second titration. The second titration with the 0.1 N $KMnO_4$ solution was stopped when the overall color of the solution abruptly changed to red (corresponding to the complete oxidation of V^{4+} to V^{5+}) and the total volume of the $KMnO_4$ solution consumed during the second titration (V2) was measured. Finally, the average oxidation state of vanadium (AV) was calculated by the equation "AV = 5 −V1/V2".

Concerning the electrochemical performance, the positive electrodes were manufactured by mixing 80 wt % active material, 10 wt % conductive carbon (Super C65, Timcal), and 10 wt % poly(vinylidene fluoride) binder (PVDF 5130, Solvay) dissolved in N-methylpyrrolidone (NMP, Aldrich). A few extra millimeters of NMP were added and the resulting slurry was stirred for 1 h. This slurry was coated on aluminum foil using the "doctor blade" technique. The electrode film was dried at 80 °C in a vacuum oven for 24 h. Circular electrodes were cut from the foil, pressed for better contact of the coated material and aluminum current collector, dried under vacuum overnight (120 °C) and finally transferred to an argon-filled glovebox (Jacomex). The mass loading of the electrodes was about 4 mg cm^{-2}. Electrochemical measurements were performed using metallic sodium as counter electrode, glass microfiber (Whatman, GF/A) as separator and a 1 M $NaPF_6$ in ethylene carbonate:dimethyl carbonate (EC:DMC, 1:1 by wt %) as electrolyte. The electrochemical cycling was performed using a Biologic VMP3 multichannel potentiostat−galvanostat. Galvanostatic cycling was performed at C/20 rate stopping at different voltages between 2.8 and 4.3 V during charge and discharge to obtain the post-mortem electrodes. The lattice parameter evolution of the extracted post-mortem cathodes were determined using XRD data collected on the Bruker D8 system.

The evolution of vanadium oxidation state during charge/discharge process was followed by X-ray absorption near-edge spectroscopy (XANES) using cycled post-mortem electrodes stopped at different steps of voltage during the electrochemical reaction. These experiments were conducted on the XAFS beamline of the Elettra Synchrotron (Trieste, Italy). XANES data were collected at the vanadium K-edge (5465 eV) in transmission mode and at room temperature, with a step size of ΔE = 0.1 eV for the edge region. Energy calibration was established by measuring simultaneously a vanadium foil inserted between the second and third ionization chambers. All the spectra were normalized by a standard procedure,[11] using Athena analysis software.[12] XAS spectra of specifically prepared V^{3+} ($Na_3V_2(PO_4)_3$ − V^{3+} standard) and V^{4+} ($Na_3V_2O_2(PO_4)_2F$ − V^{4+} standard) standards were also measured for reference. These standards were prepared such that there structures were similar to that of the studied samples, in order to improve the XANES analysis. No standard with a structure resembling that of the studied samples could be obtained for V^{5+}.

3. RESULTS AND DISCUSSION

3.1. Characterization of the Raw Mixed-Valence $Na_3V_2O_{2x}(PO_4)_2F_{3-2x}$ Sample. The hydrothermal synthesis of $Na_3V_2O_{2x}(PO_4)_2F_{3-2x}$ resulted in a black powder, suggesting that some carbon remains in the material after synthesis. This is confirmed by elemental analysis, which shows that 6.40 ± 0.05 wt % of carbon remains in the final product. The sample was examined by XRD, showing well-defined diffraction maxima, indicating a crystalline sample, with a small amount of unreacted VPO_4 initial precursor (see Figure 1). The diffraction pattern was indexed to a phase adopting $P4_2/mnm$ space group symmetry with lattice parameters a = 9.030(3) Å and c = 10.644(7) Å, which are intermediate between the extreme
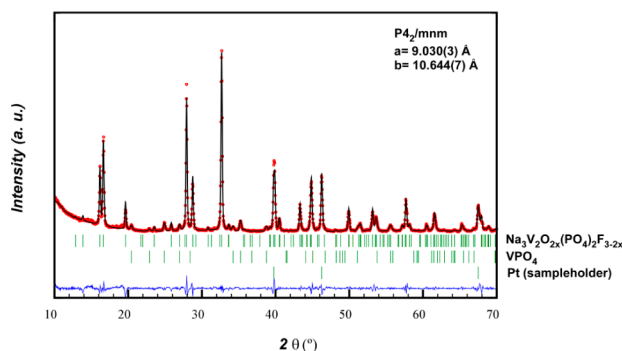
Figure 1. Whole pattern matching of XRD data of the synthesized material. Experimental (red circles), fitted (black line), and difference between them (blue lower line).

compositions of the $Na_3V_2O_{2x}(PO_4)_2F_{3-2x}$ family: $Na_3(VO)_2(PO_4)_2F$ ($x = 1$; $a = 9.03051(2)$ Å, $c = 10.62002(3)$ Å[13]) and $Na_3V_2(PO_4)_2F_3$ ($x = 0$; $a = 9.047(2)$ Å, $c = 10.705(2)$ Å[14]). The use of Vegard's law to calculate the average vanadium oxidation state results in a value of approximately $V^{3.82+}$.

To precisely determine the crystal structure of the as-synthesized material, high-resolution synchrotron XRD data were collected. Rietveld refinements were undertaken with several structural models, and the starting model of Le Meins et al.[14] gave the best initial fit to the data. This model was modified to the synthetic composition, and refined starting with the lattice followed by the atomic positional parameters. Next, the atomic isotropic displacements parameters were independently refined, and finally the occupancy of the two Na crystallographic sites. A small amount of the VPO_4 secondary phase was also present in this sample and was modeled in *Cmcm* space group with refined lattice parameters of $a = 5.2404(5)$, $b = 7.7782(7)$, and $c = 6.2858(6)$ Å. The phase fractions of VPO_4:$Na_3V_2O_{2x}(PO_4)_2F_{3-2x}$ were 2.1(6)%:97.9(1)%. The final fit to the data is shown in Figure 2, refined structural details are presented in Table 1, and the structure is shown in Figure 3.

These data suggest there is little exchange between the two Na sites. In other words, Na ions do not average out to 75% occupancy on the two available crystallographic sites (Na(1) and Na(2)), but rather one site (Na(1)) is fully occupied while the other site (Na(2)) is only half-occupied. The Na(1) site shows a large isotropic atomic displacement parameter, suggesting that the Na ions are weakly centered at this atomic site.

The distribution of F and O on the anionic sites is difficult to determine, because of the very similar scattering factors of these atoms when XRD data are used. Thus, the bond valence sum (BVS) approach[15,16] was employed, showing that the BVS for the F(1) and F(2) sites were close to 1, which is the expected value for F. In addition, the BVS for the O sites were found to be close to 2, in agreement with the BVS expected for O. However, there exists the possibility of anion disorder on these sites, which would manifest as a larger atomic displacement parameter directed to the V site, because of the variation in bond lengths between V—O and V—F. The F(1) site is the corner-connecting site for the two corner-connected vanadium octahedra and shows the largest bond length between V and any anion in this cathode. Thus, the F(1) site is an unlikely site for anion disorder. The F(2) site is "open" to the Na-ion channels and shows a large isotropic atomic displacement
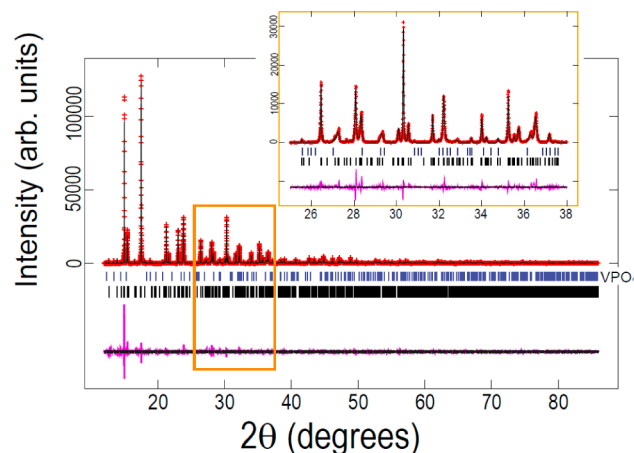

Figure 2. Rietveld refined fit of the $Na_3V_2O_{2x}(PO_4)_2F_{3-2x}$ model to the synchrotron XRD data with the inset showing an enlarged $25° \leq 2\theta \leq 38°$ region. Data are shown as crosses, the calculated Rietveld model as a line through the data, and the difference between the data and the model as the line below the data. The vertical reflection markers are for $Na_3V_2O_{2x}(PO_4)_2F_{3-2x}$ (lower markers) and VPO_4 (upper markers).

parameter, indicating F/O disorder on this site. In addition, the V—F(2) bond length is significantly smaller than the other V—O and V—F bond lengths, which suggests that some of the oxygen on this site is double-bonded to vanadium. In fact, the V—F(2) distance, 1.741(4) Å (see Table S1 in the Supporting Information), is intermediate between a single V—F bond (~2.1 Å in the V^{3+} extreme phase, end-member) and a V=O double bond (1.64 Å in the V^{4+} extreme phase, end-member), confirming the partial substitution of F by O. Calculations on the amount of F and O extrapolated from this bond length, and assuming only V=O and V—F bonds (i.e., no V—O bonds in V—F(2)), indicate a ratio of 23% F and 77% O. This corresponds to 23% V^{3+} and 77% V^{4+} and an average vanadium oxidation state of $V^{3.77+}$ on par with the vanadium oxidation state calculated from Vegard's law.

Figure 4 shows the ^{23}Na solid-state NMR (ssNMR) spectrum of the mixed-valence compound. Three main signals are present in the spectrum, which were fitted using the DMfit program.[17] The relative intensities of the resonances observed at 74, 111, and 158 ppm amount to 72%, 22%, and 6%, respectively. These shifts indicate the presence of hyperfine interactions between the ^{23}Na and the paramagnetic V ions.[18] Hyperfine shifts are very sensitive to interatomic distances, bond angles, and the oxidation states of the paramagnetic centers, and they are usually reflected by very large chemical shift values. In our case, by close examination of the coordination sphere of the Na sites, we detect that each Na^+ is in the vicinity of two equidistant V ions, as highlighted by the dashed lines in Figure 4. V^{3+} ions generally cause a more positive chemical shift than V^{4+}, by several tenths of ppms,[5,19] and their effect is additive. Based on these observations, we assign the three signals observed in the spectrum to the V^{4+}–V^{4+} (74 ppm), V^{3+}–V^{4+} (111 ppm), and V^{3+}–V^{3+} (158 ppm) pairs. Considering the relative populations of the three pairs as obtained by the fitting of the NMR spectrum (see Figure 4), we obtain an average oxidation state of the vanadium in the mixed phase of $V^{3.83+}$. For a completely random distribution of the vanadium oxidation states in a sample with an average oxidation state of +3.83, we would expect relative intensities of the V^{4+}–

Table 1. Refined Crystallographic Parameters for $Na_3V_2O_{2x}(PO_4)_2F_{3-2x}$

atom	x	y	z	site occupancy factor	isotropic atomic displacement parameter ($\times 100/Å^2$)	bond valence sum
Na(1)	0.5249(8)	0.2185(9)	0	0.973(11)	4.50(32)	0.94
Na(2)	0.7659(13)	0.0127(11)	0	0.547(9)	1.43(29)	1.10
V(1)	0.24776(23)	0.24776(23)	0.19503(10)	1	0.55(2)	3.36
P(1)	0	0.5	0.25	1	0.69(28)	4.52
P(2)	0	0	0.2556(7)	1	0.72(28)	5.23
O(1)	0.0925(7)	0.3980(8)	0.1597(10)	1	0.76(27)	2.06
O(2)	0.0946(8)	0.0946(8)	0.1644(16)	1	0.60(40)	2.16
O(3)	0.4003(8)	0.4003(8)	0.1723(16)	1	1.30(40)	2.13
F(1)	0.2489(8)	0.2489(8)	0	1	1.38(10)	1.25
F(2)	0.2504(7)	0.2504(7)	0.35865(33)	1	3.57(10)	1.24
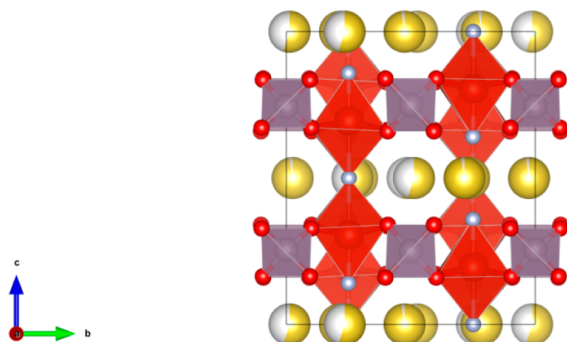
Figure 3. Crystal structure of $Na_3V_2O_{2x}(PO_4)_2F_{3-2x}$, with PO_4 shown in purple and VO_4F_2 in red. Oxygen is red, fluorine is light blue, and sodium is yellow, with the shading indicating occupancy.
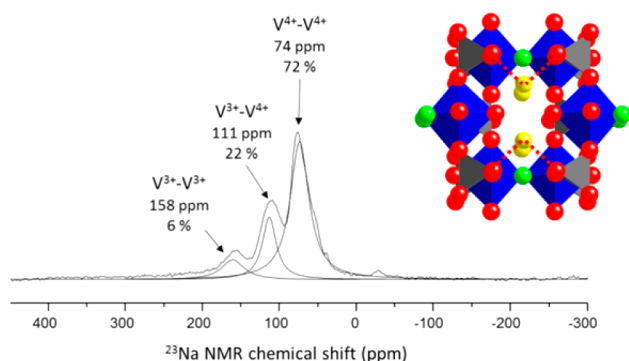
Figure 4. ^{23}Na ssNMR of the mixed-valence $Na_3V_2O_{2x}(PO_4)_2F_{3-2x}$ phase. Lines of fit are also shown. The inset on the right-hand side illustrates the equidistant V sites around Na (dashed line).

V^{4+}, $V^{3+}-V^{4+}$, and $V^{3+}-V^{3+}$ pairs of 69%, 28%, and 3%, respectively. These values are very similar to those observed in this measurement. In our case, the relative populations of the homogeneous pairs $V^{4+}-V^{4+}$ and $V^{3+}-V^{3+}$ are slightly favored, relative to the intermediate $V^{3+}-V^{4+}$ pairs. It is conceivable that the local structural changes induced by the oxidation state of one V atom can affect the stability of its neighbor.

The ^{19}F ssNMR spectrum of the compound is shown in Figure 5. The best fit of the signal was obtained by considering two Lorentzian functions centered at 109 and 94 ppm. Taking into account that the theoretical populations of the two distinct ^{19}F sites in the pure V^{3+} compound is 1:2 and the relative intensities of the two signals, we obtain a ratio of 80% V^{4+} and 20% V^{3+} in the mixed-valence phase ($V^{3.8+}$, on average). The discrepancy between the composition of the phase obtained from the ^{19}F and ^{23}Na analyses is very small ($V^{3.8+}$ and $V^{3.83+}$)
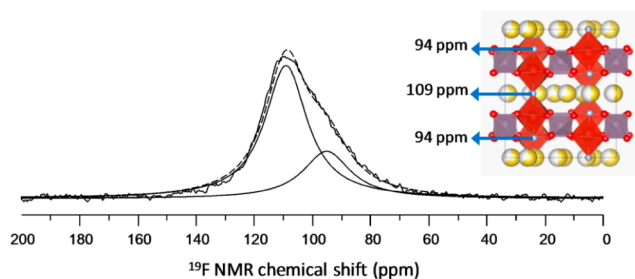
Figure 5. ^{19}F ssNMR spectrum of the mixed-valence $Na_3V_2O_{2x}(PO_4)_2F_{3-2x}$ phase. Lines of fit are also shown. The inset on the right-hand side illustrates the atomic positions of some F atoms resulting in these shifts.

and is considered to be within the error of the fitting procedures. These values are consistent with those expected from a Vegard-type relationship and the high-resolution synchrotron XRD data.

The initial vanadium oxidation state is crucial in interpreting the electrochemical Na extraction/insertion mechanism, thus another method was used to verify the vanadium oxidation state of the mixed-valence sample: the double titration method as recently employed by Park et al.[5] Moreover, different vanadium oxides (V_2O_3, VO_2, and V_2O_5) and the $Na_3V_2O_2(PO_4)_2F - V^{4+}$ standard have been also analyzed in order to have reference standards for the mixed-valence phase.

The results shown in Table 2 indicate that the mixed-valence sample is composed of 76% V^{4+} and 24% V^{3+}. Although some

Table 2. Experimentally Determined Vanadium Oxidation States for Selected Vanadium-Containing Compounds by the Double Titration Method

sample	theoretical oxidation state of vanadium	experimental average oxidation state of vanadium (AV)
V_2O_3	+3	3.04
VO_2	+4	3.98
V_2O_5	+5	5
$Na_3V_2O_{2x}(PO_4)_2F_{3-2x}$	?	3.76
$Na_3V_2O_2(PO_4)_2F - V4$ standard	+4	4.01

VPO_4 impurity remains in the cathode, this can be accounted for and is ~2% from synchrotron XRD data, so that the vanadium oxidation state for the $Na_3V_2O_{2x}(PO_4)_2F_{3-2x}$ sample remains around $V^{3.8+}$, correlating well with the other analysis techniques. In light of these data, we can propose

$Na_3V_2O_{1.6}(PO_4)_2F_{1.4}$ as the general formula for the as-synthesized material.

3.2. Post-Mortem Electrodes of $Na_3V_2O_{2x}(PO_4)_2F_{3-2x}$. We recently reported that the $Na_3V_2O_{2x}(PO_4)_2F_{3-2x}$ sodium–vanadium fluorophosphates present excellent electrochemical properties such as high specific capacity near the theoretical value and excellent cyclability.[4,6] The electrochemical behavior of the $Na_3V_2O_{2x}(PO_4)_2F_{3-2x}$/C composite has been investigated by galvanostatic cycling with periodic current interruptions (Figure 6). Prior to cycling in Galvanostatic
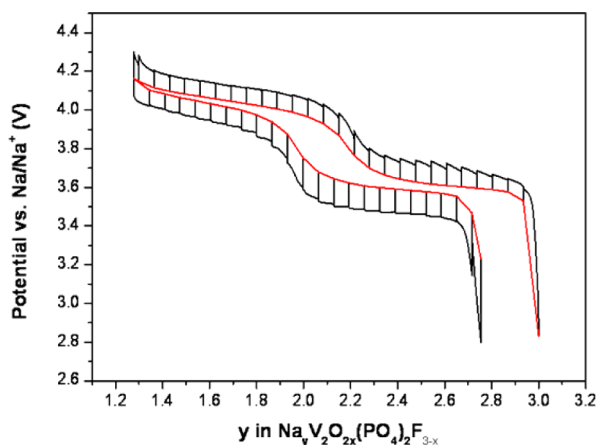

Figure 6. Galvanostatic cycle obtained in open-circuit voltage conditions (C/20 rate, relaxation criteria: 2 h). Black: experimental points. Red: curve rebuilt from relaxation points.

Intermittent Titration Technique (GITT) mode, the material has undergone three cycles at C/20 between 2.8 V and 4.3 V. The electrochemical charge–discharge curve presents two pseudo-plateaus of similar length at 3.6 V and 4.1 V vs Na/Na⁺. A discharge capacity of 98 mA h g⁻¹ (~75% of the theoretical capacity) is obtained and a low polarization was observed. The shape of the electrochemical curve suggests that the electrochemical reaction occurs through single-phase mechanisms, e.g., sloping potential curve. Similar observations have been made Chihara et al.[20] and Shakoor et al.,[6] who have investigated the electrochemical mechanism of sodium extraction/insertion from/into $Na_3V_2(PO_4)_2F_3$. Both groups report that the electrochemical reaction occurs through single-phase mechanism with negligible (~2%) volume variation.

The structural evolution of cathode materials during sodium insertion/extraction is an indicator of the long-term stability of the electrode (e.g., volume expansion/contraction and performance) or potential characteristics of the battery (e.g., solid-solution or two-phase mechanism of sodium insertion/extraction). Electrode-containing test cells were equilibrated at the potentials indicated in Figure 7 and extracted from these test cells for post mortem or ex situ XRD and XANES analysis.

Ex situ XRD data collected on electrodes extracted from Swagelok cells may react with the atmosphere to produce new phases. Although contact with air was minimized, we noted the presence of $Na_{0.29}VOPO_4 \cdot 1.73H_2O$ in some extracted electrodes, especially the electrodes at higher states of charge. In addition, we also found minute quantities of AlF_3, which is probably due to the corrosion of the Al current collector. Nonetheless, the major phase present in all extracted samples was $Na_yV_2O_{2x}(PO_4)_2F_{3-2x}$ and this was analyzed in terms of lattice parameters, which are shown in Table 3 and Figure 8.
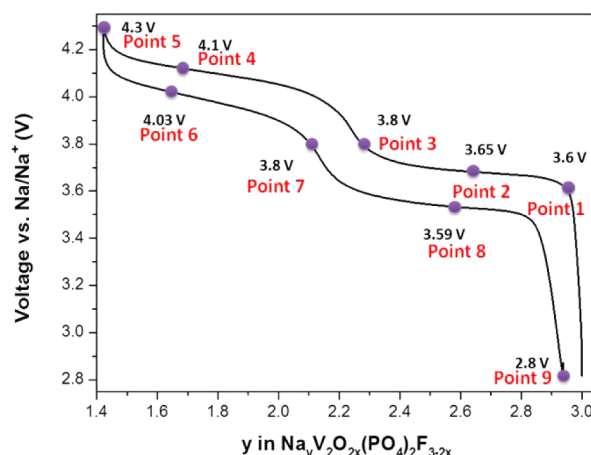

Figure 7. Points during charge/discharge where post-mortem electrodes were extracted for their analysis by XRD and XANES.

Table 3. Evolution of Lattice Parameters of the $Na_yV_2O_{2x}(PO_4)_2F_{3-2x}$ Cathode during Charge (C)/Discharge (D)

charge or discharge?	sample	a (Å)	c (Å)
	starting material	9.030(3)	10.644(7)
C	~3.6 V	9.02(1)	10.63(2)
C	~3.65 V	8.95(2)	10.70(3)
C	~3.8 V	8.92(1)	10.71(2)
C	~4.1 V	8.914(6)	10.73(1)
C	~4.3 V	8.910(4)	10.74(1)
D	~3.8 V	8.923(8)	10.71(1)
D	~3.59 V	8.96(1)	10.68(2)
D	~2.8 V	9.023(8)	10.63(1)

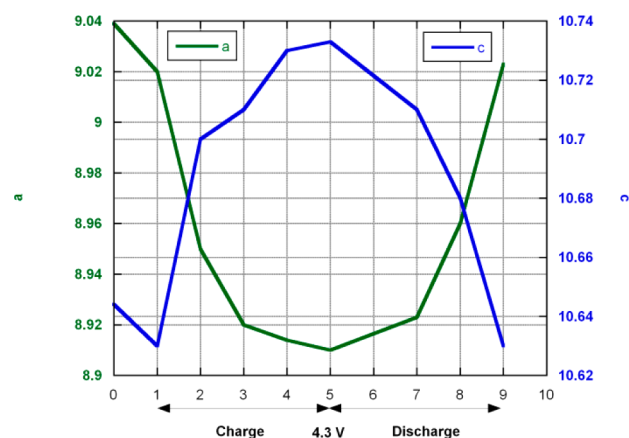**Figure 8.** Lattice parameter evolution of $Na_yV_2O_{2x}(PO_4)_2F_{3-2x}$ during charge and discharge from XRD data on post-mortem electrodes where 1 to 9 on the x-axis refers to the points in the electrochemical charge/discharge curve shown in Figure 7

There is no evidence for two-phase behavior (e.g., reflection splitting) for any of the extracted electrodes in the equilibrated state. The reflections positions shift to different 2θ values, indicating an expansion and contraction of the lattice, consistent with a solid-solution type structural evolution during charge/discharge. As shown in Table 3, lattice parameter a decreases while lattice parameter c increases during charge. This process reverses during discharge. The overall lattice volume follows the same trend as parameter a during charge/discharge.

The changes in lattice parameters a and c suggest that the tunnels in this structure evolve as shown in Figure 9 with sodium extraction during charge.
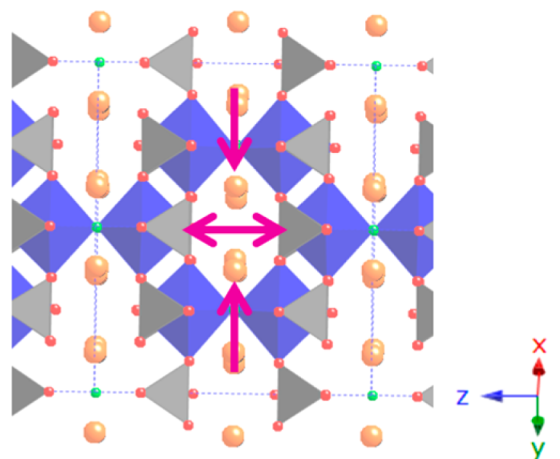

Figure 9. Evolution of the sodium channel size with charging (sodium extraction).

To confirm the evolution of the Na-ion tunnels in the crystal structure with charge/discharge, another electrode was equilibrated at point "4.1 V" during charge and high-resolution synchrotron XRD data were collected. A similar approach to the as-synthesized cathode was used to analyze the sodium-extracted electrode and the fit of the structural model to the data is shown in Figure 10, crystallographic details presented in Table 4 and the structural model shown in Figure 11.
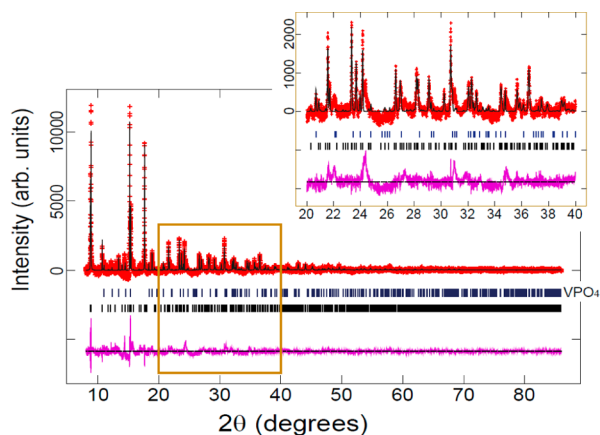

Figure 10. Rietveld refined fit of the $Na_yV_2O_{2x}(PO_4)_2F_{3-2x}$ model, where $y = 2.26(6)$ to the synchrotron XRD data with the inset showing an enlarged $20° \leq 2\theta \leq 40°$ region. Data are shown as crosses, the calculated Rietveld model as a line through the data, and the difference between the data and the model as the line below the data. The vertical reflection markers are for $Na_yV_2O_{2x}(PO_4)_2F_{3-2x}$ (lower markers) and VPO_4 (upper markers).

The refined lattice parameters were $a = 8.92220(8)$ Å and $c = 10.74862(19)$ Å, correlating to the expectations from laboratory XRD data. The sodium content was refined to 2.26(6), thus $y = 2.26(6)$ in $Na_yV_2O_{2x}(PO_4)_2F_{3-2x}$. The F(1)−F(1) and F(2)−F(2) distances, 6.363(9) and 3.008(5) Å for the as-synthesized $Na_3V_2O_{2x}(PO_4)_2F_{3-2x}$ sample and 6.3082(1) and 3.2940(1) Å for the post-mortem sample, respectively. These distances

correspond to the vertical and horizontal dimensions of the tunnels (Figure 12), and these tunnels evolve as predicted from the lattice parameters of the post-mortem electrodes, so the hypothesis of the tunnels becoming smaller in the x- and y-directions and wider in the z-direction is further confirmed.

The post-mortem synchrotron XRD data show some further noteworthy aspects. The phase fractions of VPO_4:$Na_{2.26(6)}V_2(PO_4)_2F_3$ are 10.2(2)%:89.8(1)%, which is slightly different from the phase fractions of the original cathode. In other words, a smaller fraction of fluorophosphate phase is observed, which can arise due to the conversion of some of the fluorophosphate phase into an amorphous, nanocrystalline, or disordered component with the oxidation process, thus being undetectable with XRD. Furthermore, other reflections were present for this post-mortem sample that were not identified using a range of known structural models, and can be seen at $2\theta \approx 24°$ and $31°$ in Figure 10.

The refined structural model shows highly distorted vanadium octahedra, which may indicate some type of structural transformation may occur at a certain stage of sodium extraction. Importantly, these data indicate that sodium is extracted from the Na(1) site (at least until this state of charge) and may actually proceed via the Na(2) "out" of the crystal structure. This is indicated by the ~50% reduction in site occupancy of the Na(1) site and the ~16% increase in site occupancy of the Na(2) site, compared to the as-synthesized cathode. In other words, the sodium moves from the Na(1) site to the Na(2) site and then out of the structure. However, other possibilities may exist here, e.g., sodium extraction from both sites simultaneously, and a second process that transfers sodium from Na(1) to Na(2). Note that the refined sodium content of $y = 2.26(6)$ is higher than the expected value from electrochemical considerations of $y = 1.51$. This could influence the above interpretation and the reasons for the differences in sodium content include cathode relaxation processes,[21] cathode polarization, chemical side reactions with exposure to air, and the overestimation of the sodium in the structural model due to the presence of extra unidentified phases.

High-resolution synchrotron XRD data suggest that there is a difference in phase composition between the fresh and cycled electrodes with a significant decrease in the content of the major $Na_yV_2O_{2x}(PO_4)_2F_{3-2x}$ phase in cycled electrodes. One mechanism to account for this apparent decrease is the conversion of the major $Na_yV_2O_{2x}(PO_4)_2F_{3-2x}$ phase to shorter-range or amorphous phases (or even nanocrystals that are virtually undetectable by XRD) during charge. In addition, the higher-than-expected sodium content in the major $Na_yV_2O_{2x}(PO_4)_2F_{3-2x}$ phase determined from the cycled ex-situ high-resolution synchrotron XRD data maybe due to this amorphous-like phase(s) containing significantly less sodium. The combination of the sodium contents of the amorphous-like and crystalline phases would result in the expected sodium content from the electrochemical process. Furthermore, the process of amorphization may be reversible during discharge, as expected by the electrochemical curves; however, further work is required to determine the role of the changes in phase composition.

The secondary phase, VPO_4, has been modeled in $Cmcm$ space group with the following lattice parameters: $a = 5.2342(4)$ Å, $b = 7.7819(6)$ Å, and $c = 6.2809(5)$ Å.

We have followed the evolution of the vanadium valence state during the charge/discharge process by means of XANES spectroscopy at the vanadium K-edge. This technique is

Table 4. Refined Crystallographic Parameters for $Na_{2.26(6)}V_2O_{2x}(PO_4)_2F_{3-2x}$

atom	x	y	z	site occupancy factor	isotropic atomic displacement parameter ($\times 100$ Å^2)	bond valence sum
Na(1)	0.5243(23)	0.2674(32)	0	0.491(19)	0.20(40)[a]	1.08
Na(2)	0.7956(20)	0.0554(20)	0	0.640(20)	0.20(40)[a]	0.92
V(1)	0.2478(7)	0.2478(7)	0.18610(27)	1	1.15(11)	3.98
P(1)	0	0.5	0.25	1	2.46(17)[b]	4.97
P(2)	0	0	0.2600(19)	1	2.46(17)[b]	3.71
O(1)	0.1181(13)	0.4161(11)	0.1722(13)	1	0.62(21)[c]	2.09
O(2)	0.0965(16)	0.0965(16)	0.1490(19)	1	0.62(21)[c]	1.92
O(3)	0.3934(16)	0.3934(16)	0.1611(18)	1	0.62(21)[c]	2.23
F(1)	0.2500(32)	0.2500(32)	0	1	4.45(26)[d]	1.26
F(2)	0.2398(20)	0.2398(20)	0.3468(9)	1	4.45(26)[d]	1.25

[a]Na sites were constrained to be equal. [b]P sites were constrained to be equal. [c]O sites were constrained to be equal. [d]F sites were constrained to be equal.
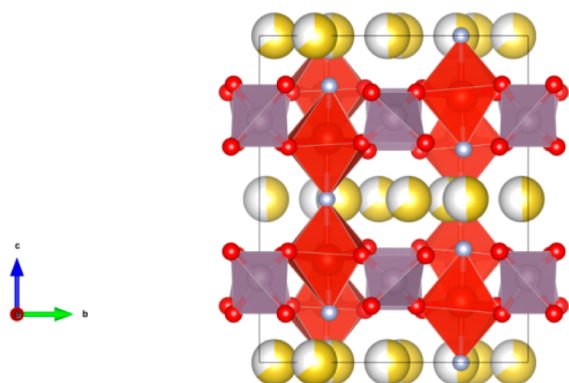

Figure 11. Crystal structure of a post-mortem electrode charged up to 4.1 V. PO$_4$ shown in purple and VO$_4$F$_2$ in red. Oxygen is red, fluorine is light blue, and sodium is yellow, with the shading indicating occupancy. The central ions in the polyhedra are shown to indicate the orientation and displacements. Crystal axes are shown inset at the bottom left.
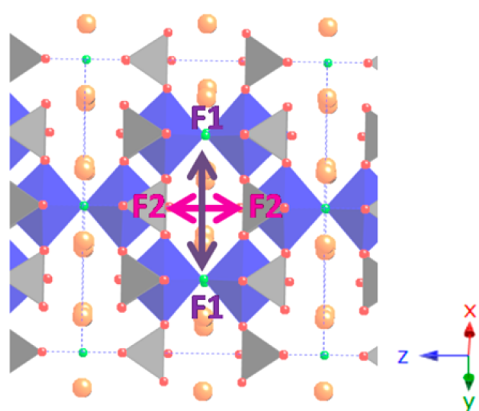

Figure 12. Evolution of F(1)−F(1) and F(2)−F(2) distances (channel size) with charging (Na extraction), according to results derived from synchrotron XRD data.

sensitive to the oxidation state and to the local structure of the absorber element (in our case, the V atom). In a qualitative way, a shift in the edge position toward higher energies with increasing vanadium valence is expected.

The XANES spectra of the post-mortem samples at different stages of the electrochemical Na extraction/insertion reaction are displayed in Figure 13. The shape of the spectra changes
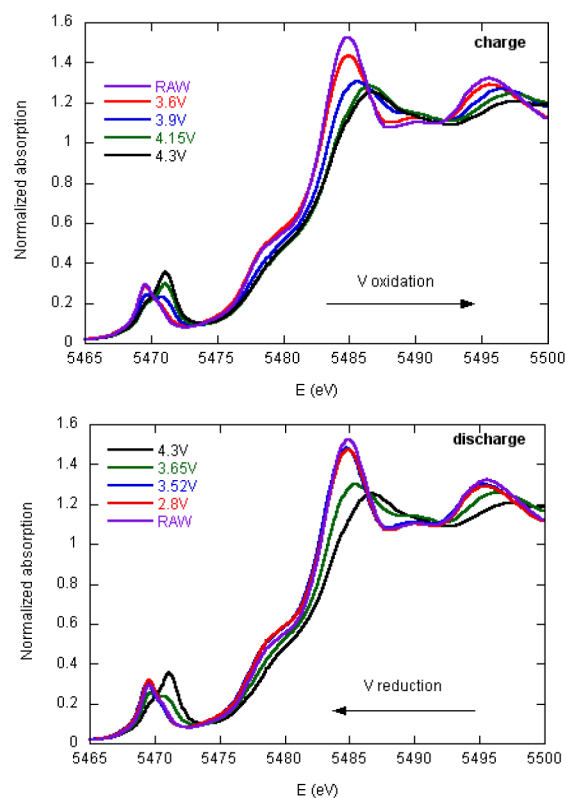

Figure 13. Vanadium K-edge XANES spectra of the samples during charge (top) and discharge (bottom).

during the charge/discharge process, as can be seen in the position of the pre-edge and white line features, which indicates changes in the vanadium environment, as revealed by XRD measurements, and in the vanadium valence state. The edge position and shape of the completely reduced sample (2.8 V) is practically identical to the as-synthesized sample (the starting Na$_3$V$_2$O$_{2x}$(PO$_4$)$_2$F$_{3-2x}$ sample, hereafter referenced as "Raw"), which indicates a complete reversibility of the charge/discharge process, at least in terms of the active vanadium oxidation states

The pre-edge feature has been assigned to a forbidden transition $1s \rightarrow 3d$.[22] The intensity and position of this feature is related to the nature and symmetry of the vanadium ligands in the sample. Figure 14 presents the evolution of the pre-edge
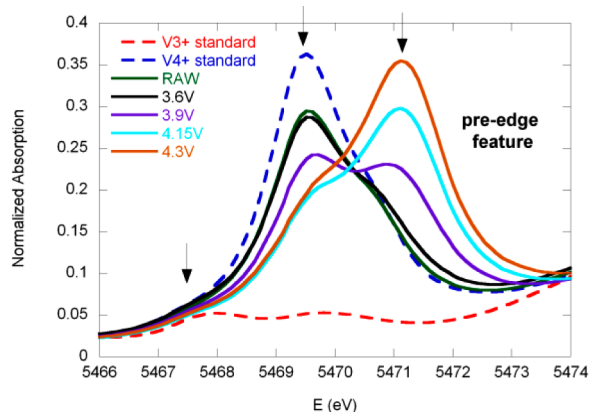

Figure 14. Vanadium K-edge pre-edge feature of the samples (continuous line) and the standards (dashed lines). Arrows indicate the position of the three characteristic peaks.

during the charge process, including $Na_3V_2(PO_4)_3 - V^{3+}$ and $Na_3V_2O_2(PO_4)_2F - V^{4+}$ standards. Closer examination reveals the presence of a triplet structure, characteristic of octahedrally coordinated vanadium cations, lacking an inversion center.[22] A qualitative analysis of this region is presented as follows: taking into account the pre-edges of our V^{3+} and V^{4+} standards, and that of V^{5+} standards according to refs 23 and 24, contributions to the pre-edge zone can be assigned to V^{3+} (5468 eV), V^{4+} (5469.5 eV), and V^{5+} (5471 eV) with increasing energy, as marked with arrows in Figure 14. As observed, during the charge process, the first peak, lowest energy V^{3+} is essentially constant. This appears to corroborate our hypothesis,[4] that V^{3+} does not participate in the oxidation process. In addition, the second peak corresponding to V^{4+} decreases, while the third peak corresponding to V^{5+} increases. This suggests that V^{4+} progressively oxidizes and converts to V^{5+}.

An estimation of the oxidation state of the raw sample can be made by fitting the pre-edge to a linear combination of the V^{3+} and V^{4+} standards.[23,24] This fitting indicates that there exists ∼82% V^{4+} and 18% V^{3+} in the as-synthesized sample, which is in good agreement with the percentage estimated by XRD, NMR, and the double titration method (∼80% V^{4+}).

To shed more light on the evolution of the vanadium valence during the oxidation/reduction of the samples, the XANES spectrum of each sample has been fitted using a linear combination of the totally reduced (Raw) and totally oxidized (4.3 V) samples.[25] The valence state of the starting sample can be obtained by fitting the XANES region to a linear combination of the V^{3+} and V^{4+} standards (see Figure S2 in the Supporting Information). This fitting indicates that there exists ∼85% V^{4+} and 15% V^{3+} in the as-synthesized sample, which is consistent with the percentage estimated by the fitting of the pre-edge (∼82% V^{4+}), as well as by the rest of the techniques employed (XRD, NMR, and double titration). Lacking a V^{5+} standard, the average oxidation state of vanadium of the 4.3 V sample was estimated from the electrochemical curve, and found to be 75.4% of oxidized material, corresponding to a $V^{4.53+}$ valence.

An example of the fitting procedure and results is illustrated in Figure 15, showing a relatively straightforward approach with
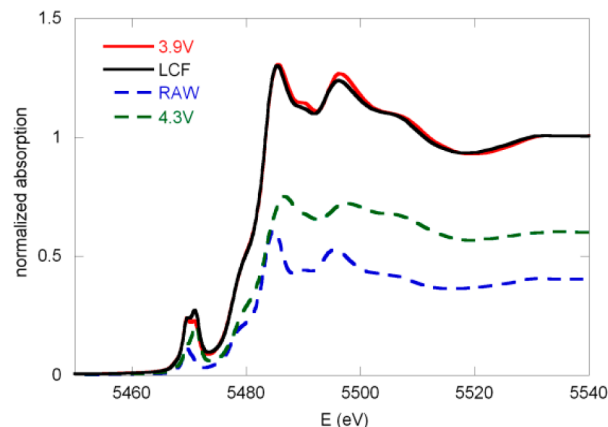

Figure 15. XANES spectra of the 3.9 V sample, and the corresponding fit to a linear combination of Raw and 4.3 V XANES profiles (LCF).

an acceptable fit. In this way, the relative amount of each component (e.g., vanadium oxidation state distribution) in all intermediate states can be determined.

Table 5 gathers the percentage of the two spectra used for the fittings: the estimated vanadium valence deduced from the

Table 5. Percentage of the Two Spectra Used for Fit XANES Data, the Estimated Vanadium Valence Obtained from the Electrochemical Curves for Each Post-Mortem Cathode, and the Vanadium Valence Calculated from the Fitting of the Spectra[a]

sample	raw spectrum (%)	C-4.3 V spectrum (%)	Vanadium Valence electrochemical curves	XANES
raw	100(5)	0(5)		3.8(1)
C-3.6 V	85(5)	15(5)	3.91	3.9(1)
C-3.9 V	40(5)	60(5)	4.14	4.2(1)
C-4.15 V	7(5)	93(5)	4.42	4.4(1)
C-4.3 V	0(5)	100(5)	4.53	4.5(1)
D-3.65 V	43(5)	57(5)	4.23	4.2(1)
D-3.52 V	100(5)	0(5)	4.1	3.8(1)
D-2.8 V	100(5)	0(5)	4.0	3.8(1)

[a]"C" indicates charge and "D" indicates discharge.

electrochemical curves for each post-mortem cathode, and the vanadium valence calculated from the fitting of the spectra. The XANES results show that, during the cathode oxidation, the average vanadium valence progressively increases from $V^{3.8+}$ to $V^{4.5+}$, and the process is completely reversible. Since the amount of V^{3+} is practically constant during the reaction, we can propose the following reaction:

$$[\text{Raw}] = 20\%V^{3+} + 80\%V^{4+}$$
$$\rightarrow [\text{Charge} - \text{``4.3 V''}] = 20\%V^{3+} + 10\%V^{4+} + 70\%V^{5+}$$
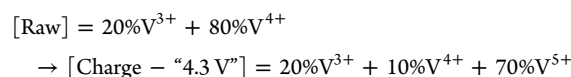
Therefore, at the end of the reaction, nearly all the V^{4+} oxidizes to V^{5+}, while the V^{3+} does not participate in the reaction.

4. CONCLUSIONS

To understand the electrochemical sodium extraction/insertion mechanism in mixed-valence compounds, the starting oxidation state of the phase and the quantity or contribution of each valence state must be first thoroughly characterized. This study employs a variety of methods including XRD, NMR, XANES, and a double titration to show the $V^{3.8+}$ oxidation state of $Na_3V_2O_{2x}(PO_4)_2F_{3-2x}$, that corresponds to 80% of V^{4+} leading to the $Na_3V_2O_{1.6}(PO_4)_2F_{1.4}$ phase. Post-mortem or ex situ XRD and XANES is then used to illustrate that (i) the sodium extraction/insertion mechanism is a solid-solution mechanism (at least in the equilibrated cathode) and (ii) mainly the V^{4+} valence is electrochemically active, transforming to V^{5+}. The V^{3+} component of the original cathode remains unchanged during electrochemical cycling in the 2.8–4.3 V range. Post-mortem analysis also indicates an anisotropic evolution of the lattice parameter during charge, with a decreasing and c increasing, and the Na-ion channels also contract in a (and b) and expand in c. Furthermore, the sodium extraction seems to occur preferentially from a particular site (Na(1)).

This study illustrates how XANES spectra can be analyzed using a combination of the completely charged and discharged samples, with the linear combinations of these represented in the intermediate states. These detailed structural studies establish the groundwork required to truly understand the sodium extraction/insertion mechanisms and to develop the best cathode materials from this family.

■ ASSOCIATED CONTENT

Ⓢ Supporting Information

Bond lengths and selected bond angles for Raw and 4.1 V post-mortem samples. Detailed XRD patterns of post-mortem electrodes during charge/discharge process. XANES spectra of the raw sample and the corresponding fit. This material is available free of charge via the Internet at http://pubs.acs.org.

■ AUTHOR INFORMATION

Corresponding Author

*Tel.: +34 946012458. Fax: +34 946013500. E-mail addresses: teo.rojo@ehu.es, trojo@cicenergigune.com.

Notes

The authors declare no competing financial interest.

■ ACKNOWLEDGMENTS

■ REFERENCES

(1) Ong, S. P.; Chevrier, V. L.; Hautier, G.; Jain, A.; Moore, C.; Kim, S.; Ma, X.; Ceder, G. *Energy Environ. Sci.* **2011**, *4*, 3680–3688.

(2) Palomares, V.; Serras, P.; Villaluenga, I.; Hueso, K. B.; Carretero-Gonzalez, J.; Rojo, T. *Energy Environ. Sci.* **2012**, *5*, 5884–5901.

(3) Yamada, A.; Chung, S. C.; Hinokuma, K. *J. Electrochem. Soc.* **2001**, *148*, A224–A229.

(4) Serras, P.; Palomares, V.; Goñi, A.; Gil de Muro, I.; Kubiak, P.; Lezama, L.; Rojo, T. *J. Mater. Chem.* **2012**, *22*, 22301–22308.

(5) Park, Y. U.; Seo, D. H.; Kim, B.; Hon, K. P.; Kim, H.; Lee, S.; Shakoor, R. A.; Miyasaka, K.; Tarascon, J. M.; Kang, K. *Sci. Rep.* **2012**, *2*, 704.

(6) Shakoor, R. A.; Seo, D.-H.; Kim, H.; Park, Y.-U.; Kim, J.; Kim, S.-W.; Gwon, H.; Lee, S.; Kang, K. *J. Mater. Chem.* **2012**, *22*, 20535–20541.

(7) Serras, P.; Palomares, V.; Goñi, A.; Kubiak, P.; Rojo, T. *J. Power Sources* **2013**, *241*, 56–60.

(8) Wallwork, K. S.; Kennedy, B. J.; Wang, D. *AIP Conf. Proc.* **2007**, 879–882.

(9) Larson, A. C.; Von Dreele, R. B. *General Structure Analysis System (GSAS)*; Report LAUR 86-748, Los Alamos National Laboratory, 1994.

(10) Toby, B. H. *J. Appl. Crystallogr.* **2001**, *34*, 210–213.

(11) Koningsberger, D.; Prins, R. *X-ray Absorption: Principles, Applications, Techniques of EXAFS, SEXAFS, and XANES*; Wiley–Interscience: New York, 1988.

(12) Ravel, B.; Newville, M. *J. Synchrotron Rad.* **2005**, *12*, 537–541.

(13) Tsirlin, A.; Nath, R.; Abakumov, A.; Fukurawa, Y.; Johnston, D.; Hemmida, M.; Krug von Nidda, H.-A.; Loidl, A.; Geibel, C.; Rosner, H. *Phys. Rev. B: Condens. Matter Mater. Phys.* **2011**, *84*, 014429.

(14) Le Meins, J.-M.; Crosnier-Lopez, M.-P.; Hemon-Ribaud, A.; Courbion, G. *J. Solid State Chem.* **1999**, *148*, 260–277.

(15) Brown, I. D.; Altermatt, D. *Acta Crystallogr., Sect. B: Struct. Sci.* **1985**, *B41*, 244–247.

(16) Brese, N. E.; O'Keeffe, M. *Acta Crystallogr., Sect. B: Struct. Sci.* **1991**, *B47*, 192–197.

(17) Massiot, D.; Fayon, F.; Capron, M.; King, I.; Le Calvé, S.; Alonso, B.; Durand, J. O.; Bujoli, B.; Gan, Z.; Hoatson, G. *Magn. Reson. Chem.* **2002**, *40*, 70–76.

(18) Grey, C. P.; Dupre, N. *Chem. Rev.* **2004**, *104*, 4493–4512.

(19) Ellis, B. L.; Ramesh, T. N.; Davis, L. J. M.; Goward, G. R.; Nazar, L. F. *Chem. Mater.* **2011**, *23*, 5138–5148.

(20) Chihara, K.; Kitajou, A.; Gocheva, I. D.; Okada, S.; Yamaki, J.-I. *J. Power Sources* **2013**, *227*, 80–85.

(21) Sharma, N.; Reddy, M. V.; Du, G.; Adams, S.; Chowdari, B. V. R.; Guo, Z.; Peterson, V. K. *J. Phys. Chem. C* **2011**, *115*, 21473–21480.

(22) Wong, J.; Lytle, F. W.; Messmer, R. P.; Maylotte, D. H. *Phys. Rev. B* **1984**, *30*, 5596–5610.

(23) Chalmin, E.; Farges, F.; Brown, G. E., Jr. *Contrib. Mineral. Petrol.* **2009**, *157*, 111–126.

(24) Farges, F. *Phys. Rev. B* **2005**, *71*, 155109.

(25) Pivko, M.; Arcon, I.; Bele, M.; Dominko, R.; Garberscek, M. *J. Power Sources* **2012**, *216*, 145–151.